# Orientation-dependent response of defective Tantalum single crystals

Diego Tramontina [a,b,c], Carlos Ruestes [a,b], Yizhe Tang [d], Eduardo Bringa [b,e,*]

[a] Agencia Nacional de Promoción Científica y Tecnológica, CABA, C1054AAH, Argentina
[b] Instituto de Ciencias Básicas, Universidad Nacional de Cuyo, Mendoza, M5502JMA, Argentina
[c] Instituto de Bioingeniería, Universidad de Mendoza, Mendoza, M5502BZG, Argentina
[d] Johns Hopkins University, Baltimore, MD 21218, USA
[e] Consejo Nacional de Investigaciones Científicas y Técnicas, CABA, C1033AAJ, Argentina

## ARTICLE INFO

## ABSTRACT

Defective Tantalum monocrystals are expected to display a particularly rich behavior when stressed along different directions. Using molecular dynamics simulations, we model Ta monocrystals containing a single spherical void of different sizes, under uniaxial compression, for two empirical potentials. Differences on the yield point, dislocation generation and plastic heating are observed depending on the void size and stress direction, as distinct slip systems are activated, resulting in a variety of dislocation structures and mobilities.

© 2014 Elsevier B.V. All rights reserved.

## 1. Introduction

Defects like dislocations, impurities, vacancies, etc., control metal plasticity, and determine applicability limits for technological applications. Voids, i.e. vacancy clusters, are ubiquitous in metals and they can arise during the manufacturing process [1,2], mechanical loading [3], or radiation damage [4,5]. Regarding mechanical loading, void nucleation is often considered the first stage of ductile fracture, and there are many studies focusing on void nucleation and growth at the nanoscale, specially for Face-Centered-Cubic (FCC) metals [6–12]. There is much less work focused on compression of nanovoids [4,13,14]. Atomistic simulations of FCC metals are carried out often partly due to large number of reliable empirical potentials for such metals [15]. Building accurate interatomic potentials for Body-Centered Cubic (BCC) metals is typically more challenging [16,17], but there is an increasing amount of work on voids in BCC metals [18–22]. Nevertheless, a large number of questions about the behavior of nanovoids under compression remain unanswered. New, detailed atomistic studies are needed in order to build reliable constitutive models which work at the nanoscale.

The mechanical behavior of materials with porosity has been treated with continuum-level constitutive model for decades, with the model by Gurson [23] leading to several improved and related models [24]. In general, these models do not take into account crystallographic orientation nor the effect of void size, with some notable exceptions [25–29]. Recent work by Bathia et al. [30] tries to improve on this for FCC Al monocrystals loaded along different directions and including voids.

In this study we also consider monocrystals but with BCC structure. Tantalum was chosen as a model BCC metal because of its technological relevance, and because it does not have thermodynamic phase transitions up to fairly high pressures and temperatures [16] unlike Iron [31]. Two different interatomic potentials are considered: the Extended Finnis–Sinclair (EFS) potential by Dai et al. [32], and the Embedded Atom Model (EAM) potential by Ravelo et al. [17]. Both potentials are of the EAM type, but we decided to call them in the above manner to be consistent with the style used by the scientific community and provide more clarity to the text. Ta monocrystals with a single void are subject to a compressive uniaxial load along the principal crystallographic directions, as an initial stage to study polycrystalline samples. Void size was systematically varied to obtain size-dependent yielding stress and compare to existing models.

## 2. Materials and methods

The simulations were performed using the molecular dynamics code LAMMPS [33]. Cubic single crystal samples with sides from 33 to 46 nm were generated with periodic boundary conditions along

all directions. A spherical void with a radius $r_v$ between 1.5 and 8 nm was introduced at the center of each sample, with the number of atoms between $2 \times 10^6$ and $6 \times 10^6$ to maintain the sample porosity below 2%. Atomic positions were relaxed using a conjugate gradient, and then were thermalized at 300 K for a few ps.

The use of nanovoids as effective dislocation sources has been extensively documented [13,19,20,34–40].

Homogeneous uniaxial compressive loading was applied to the samples, at a strain rate of $10^9 \, s^{-1}$. Atomistic simulations, where the integration time step typically is 1 fs, are limited to high strain rate loading. Such high strain rate is appropriate to study materials under shock waves, but it might also help understanding cases where other long-time scale events, like many thermally activated processes, could be neglected.

In order to study the effect of crystal orientation on plasticity mechanisms, loading was applied along the three principal crystallographic orientations, namely $\langle 100 \rangle$, $\langle 110 \rangle$ and $\langle 111 \rangle$. All simulations were carried out within the micro-canonical ensemble, monitoring the temperature evolution during the simulation to detect plastic heating. Dislocations emitted from a single void reached the periodic boundaries 1–3% strain after the initial nucleation. Larger strains are representative of a periodic array of closely spaced voids.

In order to evaluate possible changes in mechanical behavior due to different interatomic potentials, an Embedded Atom Model (EAM) potential for Ta by Ravelo et al. [17], was compared to the Extended Finnis–Sinclair (EFS) potential developed by Dai et al. [32]. Both potentials were fitted to high pressure results, as required for this study, but the EFS potential displays an artificial thermodynamic phase transition at $\sim 70$ GPa [17]. The stress in our study is always well below that transition.

Visual analysis and rendering was carried out using Ovito [41] and VMD [42]. The Crystal Analysis Tool (CAT) developed by Stukowski et al. [43] was used to calculate dislocation densities, and detect other defects like vacancies and twins.

Since the material studied here is a single crystal of cubic BCC structure, for every potential the elastic behavior is described by the corresponding elastic constants, $C_{11}$, $C_{12}$ and $C_{44}$. Several relationships between the elastic constants can be defined as follows:

The bulk modulus $B$, is defined as:

$$B = \frac{C_{11} + 2C_{12}}{3} \tag{1}$$

The Reuss-averaged shear modulus, $G_{Reuss}$, is defined as

$$G_{Reuss} = \frac{5(C_{11} - C_{12})C_{44}}{4C_{44} + 3(C_{11} - C_{12})} \tag{2}$$

The Voigt-averaged shear modulus, $G_{Voigt}$, is defined as

$$G_{Voigt} = \frac{C_{11} - C_{12} + 3C_{44}}{5} \tag{3}$$

The averaged shear modulus, $G$, is defined as the arithmetic mean over the Voigt-averaged and Reuss-averaged shear moduli

$$G = \frac{1}{2}(G_{Voigt} + G_{Reuss}) \tag{4}$$

Poisson's ratio, $v$, is defined as

$$v = \frac{3B - 2G}{2(G + 3B)} \tag{5}$$

Based on these quantities, we can define the Elastic modulus, $E$, as

$$E = 2G(v + 1) \tag{6}$$

While these calculations are very important for materials science in general, they fail to evidence the anisotropic behavior

suggested by the stiffness matrix. Therefore, we define $X$, the elastic anisotropy, as

$$X = \frac{2C_{44}}{C_{11} - C_{12}} \tag{7}$$

Finally, based on Meyers and Chawla [44], we can extract the orientation dependent elastic modulus by means of the following set of equations:

$$\frac{1}{E_{100}} = \frac{C_{11} + C_{12}}{(C_{11} + 2C_{12})(C_{11} - C_{12})} \tag{8}$$

$$\frac{1}{E_{110}} = \frac{C_{11}}{2(C_{11} + C_{12})(C_{11} - C_{12})} + \frac{1}{8C_{44}} \tag{9}$$

$$\frac{1}{E_{111}} = \frac{C_{11} + 2C_{12} + C_{44}}{3(C_{11} + 2C_{12})C_{44}} \tag{10}$$

The results for Eqs. (1)–(10) are summarized in Table 1. It must be noted that the EFS potential shows elastic moduli somewhat larger than the EAM potential, and more in agreement with experiments ($C_{11} = 264$ GPa, $C_{12} = 160$ GPa and $C_{44} = 82$ GPa) [45].

Orowan [46] expressed the plastic strain rate $\dot{\gamma}_p$, in terms of dislocations density $\rho$, and mean dislocation velocity $\bar{v}$, as:

$$\dot{\gamma}_p = b\rho_m \bar{v} \tag{11}$$

where $b$ is the Burgers vector. Swegle and Grady [47] considered a modified equation particularly useful for high strain rate loading,

$$\dot{\gamma}_p = \frac{d\rho}{dt} b\bar{l} \tag{12}$$

where $\bar{l}$ is the average distance new dislocations move.

The temperature rise associated with plastic deformation can be expressed in a simplified fashion as:

$$\frac{dT}{dt} = \frac{\beta}{C}\tau(t)\dot{\gamma}_p \tag{13}$$

where $C$ is the specific heat capacity, $\tau(t)$ is the time dependent shear stress, and $\beta$ is an empirical parameter that represents the fraction of plastic work dissipated as heat [48].

## 3. Results

Fig. 1(a and d) shows the stress–strain curves for the each load direction and both potentials. As expected after the calculations shown in Table 1, the elastic behavior shown for each potential and each loading direction differs according to the orientation dependent elastic moduli. For instance, for [100] loading, the corresponding elastic modulus is higher for the EAM potential, while the EFS potential gives a higher modulus for [100] and [110] loading. This explains the different slopes in Fig. 1(a and d).

The large stress variation amongst the different crystalline directions in Fig. 1(a and d) is mostly due to elastic anisotropy. If we use $S_{VM}/E_{hkl}$, taking into account possible pressure induced

**Table 1**
Elastic constants and bulk properties calculated with Eqs.(1)–(10) for the EAM and EFS interatomic potentials at zero pressure. Experimental values for the elastic constants and the resulting calculated variables are also given ($C_{11} = 264$ GPa, $C_{12} = 160$ GPa and $C_{44} = 82$ GPa) [45].

| Quantity | EFS | EAM | Quantity | EFS | EAM |
|---|---|---|---|---|---|
| $C_{11}$ (GPa) | 203.8 | 262.6 | $v$ | 0.325 | 0.345 |
| $C_{12}$ (GPa) | 143.5 | 160.7 | $E$ (GPa) | 180 | 181 |
| $C_{44}$ (GPa) | 91.3 | 81.8 | $X$ | 2.09 | 1.66 |
| $B$ (GPa) | 172.6 | 194.6 | $E_{100}$ (GPa) | 120 | 140 |
| $G_{Reuss}$ (GPa) | 63.5 | 65.8 | $E_{110}$ (GPa) | 204 | 191 |
| $G_{Voigt}$ (GPa) | 72.2 | 69.5 | $E_{111}$ (GPa) | 231 | 215 |
| $G$ (GPa) | 67.9 | 67.2 | | | |
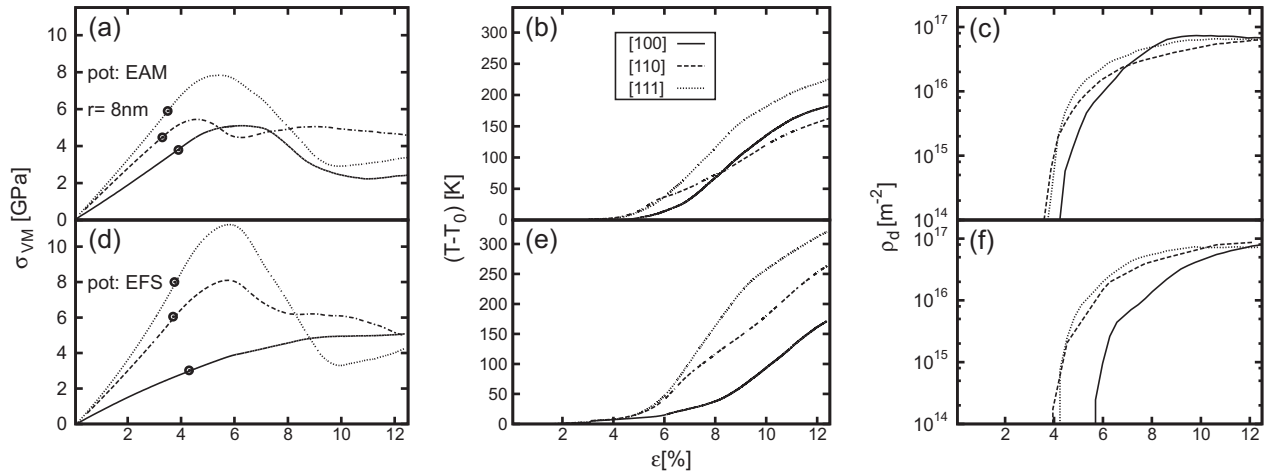
**Fig. 1.** Loading of a void with $r_v = 8$ nm, for an initial box size of $(32 \times 32 \times 32)$ nm$^3$. Different loading directions as indicated in boxed label. *First row*, EAM potential [17]; *second row*, EFS potential [32]. *First col.*: Stress–strain curves, using von Mises stress. Plastic yielding $\sigma_y$ is indicated with dots. *Second col.*: Temperature change, $T - T_0, T_0 = 300$ K; there is a large temperature increase due mostly to plastic heating for strains above plastic yielding. *Third col.*: Dislocation density, reaching similar saturation density independently of loading direction or interatomic potential.

**Table 2**
EFS: Resolved shear stresses on the 12 slip systems corresponding to families of {110} slip planes and 12 slip systems for families of {112} slip planes; for uniaxial strain compression along [001].

| Slip plane | RSS (GPa) | Slip systems |
|---|---|---|
| {110} | 35.6 $\epsilon_{33}$ | $(011)[11\bar{1}]\ (011)[\bar{1}1\bar{1}]\ (01\bar{1})[111]\ (01\bar{1})[\bar{1}11]$ |
| | | $(101)[11\bar{1}]\ (101)[1\bar{1}\bar{1}]\ (10\bar{1})[111]\ (10\bar{1})[1\bar{1}1]$ |
| | 0 | $(110)[1\bar{1}\bar{1}]\ (110)[\bar{1}1\bar{1}]\ (1\bar{1}0)[111]\ (1\bar{1}0)[11\bar{1}]$ |
| {112} | 41.1 $\epsilon_{33}$ | $(112)[11\bar{1}]\ (\bar{1}12)[\bar{1}1\bar{1}]\ (1\bar{1}2)[1\bar{1}\bar{1}]\ (11\bar{2})[111]$ |
| | 20.6 $\epsilon_{33}$ | $(1\bar{2}1)[111]\ (\bar{2}11)[111]\ (211)[\bar{1}11]\ (12\bar{1})[1\bar{1}1]$ |
| | | $(21\bar{1})[1\bar{1}1]\ (121)[1\bar{1}1]\ (\bar{1}21)[11\bar{1}]\ (2\bar{1}1)[11\bar{1}]$ |

**Table 3**
EFS: Resolved shear stresses on the 24 slip systems corresponding to the family of {123} slip planes; for uniaxial strain compression along [001].

| Slip plane | RSS (GPa) | Slip systems |
|---|---|---|
| {123} | 40.4 $\epsilon_{33}$ | $(123)[11\bar{1}]\ (\bar{1}23)[\bar{1}1\bar{1}]\ (12\bar{3})[1\bar{1}\bar{1}]\ (12\bar{3})[111]$ |
| | | $(213)[11\bar{1}]\ (\bar{2}13)[1\bar{1}1]\ (2\bar{1}3)[\bar{1}11]\ (21\bar{3})[111]$ |
| | 26.9 $\epsilon_{33}$ | $(312)[\bar{1}11]\ (\bar{3}12)[111]\ (3\bar{1}2)[11\bar{1}]\ (31\bar{2})[1\bar{1}1]$ |
| | | $(132)[1\bar{1}1]\ (\bar{1}32)[11\bar{1}]\ (13\bar{2})[111]\ (13\bar{2})[\bar{1}11]$ |
| | 13.5 $\epsilon_{33}$ | $(231)[1\bar{1}1]\ (\bar{2}31)[11\bar{1}]\ (23\bar{1})[111]\ (23\bar{1})[\bar{1}11]$ |
| | | $(321)[\bar{1}11]\ (\bar{3}21)[111]\ (3\bar{2}1)[11\bar{1}]\ (32\bar{1})[1\bar{1}1]$ |

modifications in $E_{hkl}$, the resulting spread is less than 1% amongst different directions.

Detailed calculations of the Resolved Shear Stress (RSS) for uniaxial compression along [001] are shown in Tables 2–5. The highest RSS corresponds to four {112}⟨111⟩ planes (41.1$\epsilon$ for EFS and 47.8$\epsilon$ for EAM). The second highest RSS corresponds to eight {123}⟨111⟩ planes (40.4$\epsilon$ for EFS and 46.9$\epsilon$ for EAM). The third highest RSS corresponds to eight {011}⟨111⟩ planes (35.6$\epsilon$ for EFS and 41.4$\epsilon$ for EAM).

The RSS calculations suggest on which planes the first slip will be activated, but do not include possible dynamic effects just before nucleations, and they are not strictly valid once plasticity begins. The RSS calculation for the single crystal would also be affected when a void is included in the sample, because local stress and slip at the void surface would be affected by other factors like local curvature and the presence of surface steps. In addition, there are several studies for BCC metals indicating that non-Schmidt effects could be important [49]. Despite all these limitations, in our simulations for [001] loading, we do observe that the first active slip plane belongs to the {112}⟨111⟩ family, in agreement with highest calculated RSS. In addition, although {123}⟨111⟩ slip has only slightly lower RSS than {112}⟨111⟩ slip, we do not observe activation of these systems during loading of voids.

Simulations for [001] loading presented here are consistent with previous results from Tang et al. and his analytical model [39]. The highest yield stress is found for the [111]-strained sample, followed by the [110] and [100]-strained samples. This follows from the elastic moduli in Table 1 and the fact that, for a given void radius and potential, samples yield at roughly the same strain, with the [110]-strained sample yielding at a slightly lower

**Table 4**
EAM: Resolved shear stresses on the 12 slip systems corresponding to families of {110} slip planes and 12 slip systems for families of {112} slip planes; for uniaxial strain compression along [100].

| Slip plane | RSS (GPa) | Slip systems |
|---|---|---|
| {110} | 41.4 $\epsilon_{33}$ | $(011)[11\bar{1}]\ (011)[\bar{1}1\bar{1}]\ (01\bar{1})[111]\ (01\bar{1})[\bar{1}11]$ |
| | | $(101)[11\bar{1}]\ (101)[1\bar{1}\bar{1}]\ (10\bar{1})[111]\ (10\bar{1})[1\bar{1}1]$ |
| | 0 | $(110)[1\bar{1}\bar{1}]\ (110)[\bar{1}1\bar{1}]\ (1\bar{1}0)[111]\ (1\bar{1}0)[11\bar{1}]$ |
| {112} | 47.8 $\epsilon_{33}$ | $(112)[11\bar{1}]\ (\bar{1}12)[\bar{1}1\bar{1}]\ (1\bar{1}2)[1\bar{1}\bar{1}]\ (11\bar{2})[111]$ |
| | 23.9 $\epsilon_{33}$ | $(1\bar{2}1)[111]\ (\bar{2}11)[111]\ (211)[\bar{1}11]\ (12\bar{1})[1\bar{1}1]$ |
| | | $(21\bar{1})[1\bar{1}1]\ (121)[1\bar{1}1]\ (\bar{1}21)[11\bar{1}]\ (2\bar{1}1)[11\bar{1}]$ |

**Table 5**
EAM: Resolved shear stresses on the 24 slip systems corresponding to the family of {123} slip planes; for uniaxial strain compression along [100].

| Slip plane | RSS (GPa) | Slip systems |
|---|---|---|
| {123} | 46.9 $\epsilon_{33}$ | $(123)[11\bar{1}]\ (\bar{1}23)[\bar{1}1\bar{1}]\ (12\bar{3})[1\bar{1}\bar{1}]\ (12\bar{3})[111]$ |
| | | $(213)[11\bar{1}]\ (\bar{2}13)[1\bar{1}1]\ (2\bar{1}3)[\bar{1}11]\ (21\bar{3})[111]$ |
| | 31.3 $\epsilon_{33}$ | $(312)[\bar{1}11]\ (\bar{3}12)[111]\ (3\bar{1}2)[11\bar{1}]\ (31\bar{2})[1\bar{1}1]$ |
| | | $(132)[1\bar{1}1]\ (\bar{1}32)[11\bar{1}]\ (13\bar{2})[111]\ (13\bar{2})[\bar{1}11]$ |
| | 15.6 $\epsilon_{33}$ | $(231)[1\bar{1}1]\ (\bar{2}31)[11\bar{1}]\ (23\bar{1})[111]\ (23\bar{1})[\bar{1}11]$ |
| | | $(321)[\bar{1}11]\ (\bar{3}21)[111]\ (3\bar{2}1)[11\bar{1}]\ (32\bar{1})[1\bar{1}1]$ |

strain than the other directions. This comparison can be seen in Fig. 2(a and b). According to these results, monocrystalline Ta behavior is not only dependent on the size of existing imperfections [38], but also on the applied stress direction, as expected [26].

In general, a higher strain is needed in order to initiate plasticity when strained along the [100] direction, due to the much smaller $E_{100}$ modulus. For the smallest void size ($\sim 1.5$ nm, a large
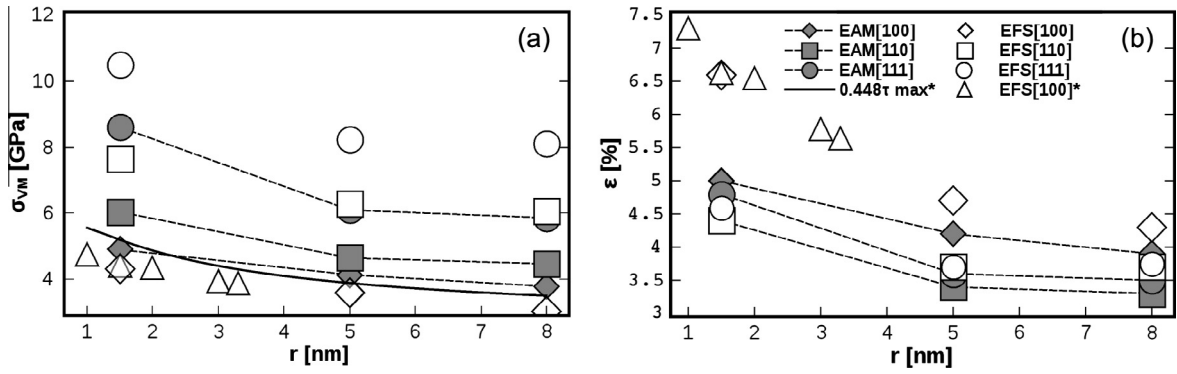
**Fig. 2.** (a) von Mises yield stress as a function of void radius for the principal BCC slip directions. Results for EAM potential [17] and EFS potential [32] are shown. Previous MD simulations from Tang et al. [39], along with their analytical model (both with an asterisk in the label caption), show good agreement with our results. (b) Dislocation nucleation strain as a function of void radius. Only EAM data are connected with lines as a guide to the eye.
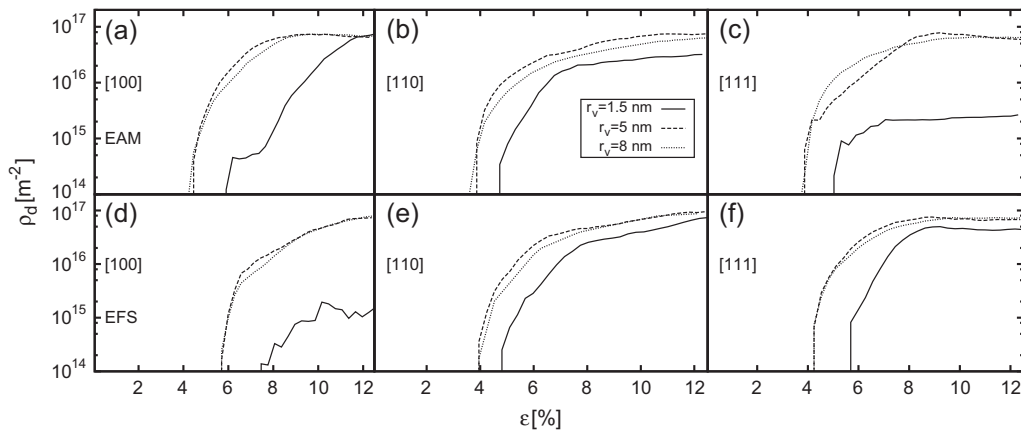


**Fig. 3.** Dislocation density as a function of strain for different void sizes. First row: EAM potential. Second row: EFS potential. As expected, dislocation emission from the smallest void requires the largest strain. Almost the same dislocation density is reached at large strains for all cases, with the exception of the smallest void for the EAM potential, [111] loading; and EFS potential, [100] loading.

difference is obtained between the yield stress values from EFS and EAM, reaching a maximum difference of ($\Delta\varepsilon \approx 2.0\%$) for the [100] stress direction. The dependency of the yield stress and yield strain on the chosen potential decreases with void radius, but this does not guarantee similarities in the resulting microstructure at higher strains.

Prior to the onset of plasticity, temperature increases only slightly during the elastic stage due to $PdV$ work. After this point, stress softening occurs, along with a more pronounced temperature increase due to the large increase in dislocation density.

The general scenario of plasticity evolution can be analyzed with the aid of Eqs. (12) and (13). In the simulations presented here the applied strain rate would be accommodated by a rapid generation of dislocations in the defect-free crystal outside the void. This plastic strain rate, related to Eq. (12), would lead to an steep increase in temperature through Eq. (13). Immediately after plastic yielding, the total dislocation density would increase by the generation of new dislocations, which then move relatively independent of each other. At higher strains dislocations would start to form junctions and eventually reach a saturation value, with the mean dislocation velocity dropping rapidly [50]. However, a small fraction of dislocations would still move and, according to Eqs. (11) and (12), lead to further temperature increase, but at a lower rate.

As displayed in Fig. 1, this scenario is somewhat confirmed in our simulations. Immediately after plastic yielding there is no large stress relaxation nor temperature increase, since dislocation motion is nearly negligible at this very early plastic stage. The next
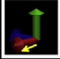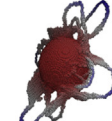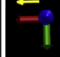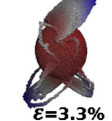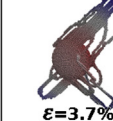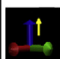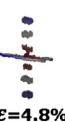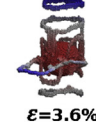
stage involves motion of those nucleated dislocations together with nucleation of new ones, leading to shear stress drop and increased plastic heating. Finally, the huge dislocation density generates many dislocation junctions slowing down dislocation motion and reducing the plastic heating rate, accompanied by a leveling-off in the shear stress.

The large $\sigma_y$ for [111] loading leads to an immense dislocation burst, which then leads to the largest temperature increase and shear stress drop. The opposite case is [001] loading, where $\sigma_y$ is the smallest and dislocation nucleation starts at a larger strain, leading to a much smaller heating rate, and a small shear stress drop for the EAM potential and no shear stress drop for the EFS potential. [011] loading sits generally in between. The cross-over between the [001] and [011] for plastic heating, has the expected counterpart in the respective dislocation densities.
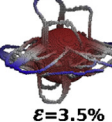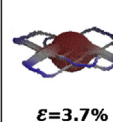
Note that the shear stress at large strains is about 4 GPa for all directions and for both potentials, and that this is likely related to a Taylor-like relationship between stress and dislocation density, since dislocation density saturates to about $6.5 \times 10^{16}$ m$^{-2}$ for all loading directions and both potentials. A Taylor relationship for forest dislocation hardening would be given by:

$$\sigma = \beta G b \rho^{1/2} \qquad (14)$$

where we can use for Ta $b = 0.286$ nm, $G \approx 67.5$ GPa from Table 1. $\beta$ is a parameter of order unity which depends on dislocation interactions, and that was taken as 0.4 within the MTS model

| | EAM | | | EFS | | |
|---|---|---|---|---|---|---|
| | r=1.5nm | r=5nm | r=8nm | r=1.5nm | r=5nm | r=8nm |
| [100] | $\varepsilon=5\%$ | $\varepsilon=4.2\%$ | $\varepsilon=3.9\%$ | $\varepsilon=6.6\%$ | $\varepsilon=4.7\%$ | $\varepsilon=4.3\%$ |
| [110] | $\varepsilon=4.4\%$ | $\varepsilon=3.4\%$ | $\varepsilon=3.3\%$ | $\varepsilon=4.4\%$ | $\varepsilon=3.7\%$ | $\varepsilon=3.7\%$ |
| [111] | $\varepsilon=4.8\%$ | $\varepsilon=3.6\%$ | $\varepsilon=3.5\%$ | $\varepsilon=4.6\%$ | $\varepsilon=3.7\%$ | $\varepsilon=3.7\%$ |

**Fig. 4.** Snapshots of the defect structures for several uniaxial stress directions, using the EAM [17] and the EFS [32] interatomic potentials. Axes are shown for each case, while the yellow arrow indicates stress direction. Coloring indicates distance from void center, with blue being further away. (For interpretation of the references to color in this figure legend, the reader is referred to the web version of this article.)

[51]. Taking a somewhat larger but still reasonable value of $\beta \approx 0.8$ gives $\sigma \approx 4$ GPa, in agreement with our MD simulations.

The high dislocation densities observed in our simulations, reaching nearly $\rho_d = 10^{17}$ m$^{-2}$, are in the upper limit of the expected values for highly work-hardened metals ($10^{15} - 10^{17}$ m$^{-2}$). High strain rate deformation is likely to produce such high dislocation densities, as shown by Nemat-Nasser et al. [52] reporting $\rho_d = 10^{17}$ m$^{-2}$ for polycrystalline Ta, and Hsiung [53] reporting $\rho_d = 10^{16}$ m$^{-2}$ for Ta under explosive-driven shocks of up to 30 GPa.

The dislocation density evolution for all simulations is observed in Fig. 3. The $r_v = 1.5$ nm void, loaded along [001] displays an initial dislocation density rise, followed by a plateu because after the first loop is nucleated, no other dislocation nucleates or moves.

As noted above, dislocation density saturates to a value of $\sim 6.5 \times 10^{16}$ m$^{-2}$ in all cases, except [001] and [111] loading of the $r_v = 1.5$ nm void, where it reaches a much lower value. Neglecting the particular case of a tiny void, one would agree with the MTS model [51], where a saturation dislocation density which depends on strain rate is considered, with a strain rate of $10^9$ s$^{-1}$ resulting in $\rho_{sat} \approx 2.5 \times 10^{16}$ m$^{-2}$, extremely close to our MD result.

A recent extension of the MTS includes twin-dislocation interaction [54]. It was argued that a much rapid dislocation multiplication, possibly 100 times faster for [001] loading than for [011] loading, would lead to much less twinning for [001] loading than for [011] loading, as observed in recovered samples [54]. For the particular cases simulated here, i.e. samples with a void as a dislocation source, nearly the same dislocation multiplication rates are observed for [001] and [011] loading. This might point out to the need for direction-dependent twin nucleation and growth mechanisms instead of such huge differences in dislocation production rates.

Despite dislocation densities being similar for loading along different directions, resulting microstructures are different, as shown in Fig. 4. For the smallest void size studied, the spread in yield stress was larger, and structures are particularly different amongst different loading directions.

In our simulations, shear loops nucleate at ledges provided by the void surfaces, as discussed by Tang et al. [38]. For [001] loading

the first slip system to become active agrees with the prediction of maximum RSS from Tables 3 and 5. As plasticity develops, the tendency of screw dislocations to cross-slip among slip systems sharing the same Burgers vector and close RSS, helps in the production of the complex structures presented, where it is clear that multiple slip systems are activated.

When comparing the interatomic potentials at the same void sizes, loop emission gets delayed for EFS when compared to EAM. This was seen in the stress strain curves, particularly for [100] loading.

Dislocation structures from uniaxial compression along [100] have been extensively explained by Tang et al. [38] using the EFS [32] potential, and has been reproduced in this document with good agreement.

If the sample is compressed along the [110] direction, preferential slipping over the {112}⟨111⟩ is observed. Loops move along four ⟨111⟩ directions to the stress, as can be seen in Fig. 4. Each structure shows the expected [38] mixed dislocation loops, with the screw portions parallel to the displacement vector and the edge components at the front.

If the sample is compressed along the [111] direction, emission of prismatic loops is observed for voids with $r_v = 1.5$ nm and 5 nm. Hagelaar et al. [55] showed an extremely similar microstructure in simulations of nanoindentation in W, for an indenter with a radius of 4 nm. Stress states should be roughly similar for the case of nanoindentation and for the cases presented here.

Planar structures seen in several pannels of Fig. 4 are {112}⟨111⟩ twins, as expected from compression of BCC metals and discussed by Tang et al. [38]. Twinning is shown in detail for [011] loading, and $r_v = 8$ nm, in Fig. 5. The initial stages of twinning follow the mechanism shown in [38]. Note also the straight shear loop bending near the tip due to cross-slip of the screw components. Fig. 5 also shows a close-up of a twin, indicating the relevant planes. Fig. 5(c and d) shows that twinning is much more prominent for the EAM potential than for the EFS potential. We note that the EAM potential by Ravelo et al. [17] was specifically fitted taking into account the twin activation threshold for Ta under high pressure and high strain rate conditions. In both cases a dislocation forest can be observed, justifying the use of a Taylor approximation to estimate flow stress.

[11-2]
[1-10]

3nm

(a)                                    (b)

[111]
[1-10]
[-1-12]

[111]
[1-10]
[-1-12]

(c)                                    (d)
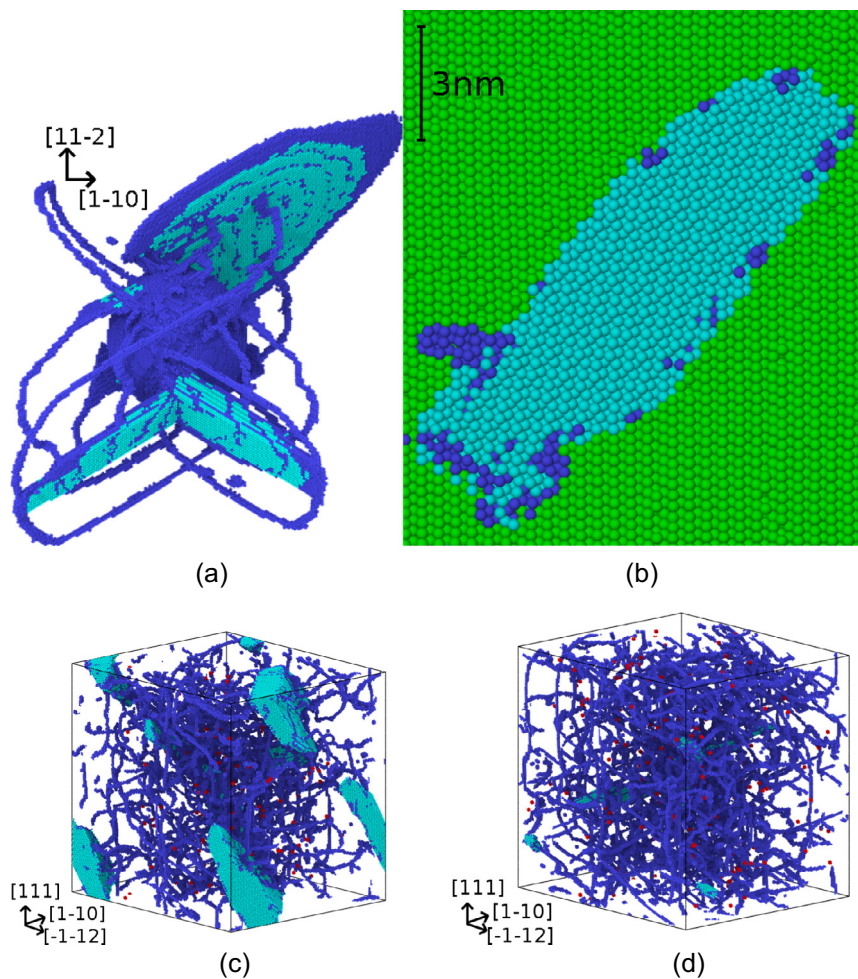
**Fig. 5.** Loading of a void with $r_v = 8$ nm, for an initial box size of $(32 \times 32 \times 32$ nm$)^3$, along [0 1 1]. Only defective atoms are shown. Teal: twinned atoms; blue: dislocation lines; red: vacancies. (a) EAM potential, at 12.3% strain. On top left, note cross-slip of screw segments, bending the tip of the shear loop still attached to the void surface. (b) EAM potential: zoom of a region of the sample showing a twin at 12.3% strain. The view is perpendicular to the (11–2) plane. Normal BCC atoms are also shown in green. (c) EAM potential, at 12.3% strain. Twin fraction is $\sim 6.3\%$, and $\rho \approx 6 \times 10^{16}$ m$^{-2}$. (d) EFS potential at 12.3% strain. Twin fraction is $\sim 0.3\%$, and $\rho \approx 7.5 \times 10^{16}$ m$^{-2}$. The void has dissapeared well before 12.3% strain for both potentials, leaving behind a dense dislocation forest. (For interpretation of the references to color in this figure legend, the reader is referred to the web version of this article.)

## 4. Summary and conclusions

Uniaxial compressive loading of Ta single crystals with a single spherical void of radius $r_v = 1.5$, 5 and 8 nm, was carried out along [0 0 1], [0 1 1] and [1 1 1] directions, using two different empirical potentials: an Embedded Atom Method (EAM) potential [17], and the Extended Finnis–Sinclair (EFS) potential [32]. As expected, our results show that the elastic loading region depends on the corresponding elastic moduli and that plasticity initiation at the void surface depends strongly on void size and loading direction, with smaller voids leading to larger plastic thresholds.

When comparing the two potentials, we found the same trends with void size and loading orientation but large differences in nucleation stress (up to $\sim 2$ GPa) and strain (up to $\sim 2\%$); the spread in the nucleation stress and strain for different loading directions is somewhat smaller for the EAM potential.

Dislocation structure does depend on void size but systematic analysis of plastic activity showed that slip systems activated for each loading direction were the same for both potentials, and that slip activation can be explained by the relevant Schmid factors.

The temperature increase associated with plastic heating differs for different loading directions, while dislocation densities are nearly the same, for strains well above plastic initiation.

Dislocation generation and multiplication was also found to be similar for different loading directions.

The study from Bathia et al. [30] on Al crystals with porosity showed that atomistic simulations can inform continuum yield models for multiscale applications. Advanced constitutive models must include effect of the porosity size distribution, and crystal anisotropy [56]. Our findings emphasize the fact that nanoscale defects have to be treated with care when incorporated into continuum models. As an example, thermodynamic state variables like temperature cannot be accurately estimated with models specifying only stress–strain state and neglecting dislocation source sizes and loading details controlling the early stages of plasticity.

## References

[1] C.C. Peng, C.K. Chung, B.H. Wu, M.H. Weng, C.C. Huang, J.F. Lin, Surf. Coat. Tech. 205 (19) (2011) 4672–4682, http://dx.doi.org/10.1016/j.surfcoat.2011.04.032.

[2] R. Nakamura, T. Shudo, A. Hirata, M. Ishimaru, H. Nakajima, Scripta Mater. 64 (2) (2011) 197–200, http://dx.doi.org/10.1016/j.scriptamat.2010.09.043.

[3] S.D. Antolovich, R.W. Armstrong, Prog. Mater. Sci. 59 (2014) 1–160. http://dx.doi.org/10.1016/j.pmatsci.2013.06.001.

[4] D.B. Reisman, W.G. Wolfer, A. Elsholz, M.D. Furnish, J. Appl. Phys. 93 (11) (2003) 8952, http://dx.doi.org/10.1063/1.1571969.

[5] M. Lambrecht, E. Meslin, L. Malerba, M. Hernández-Mayoral, F. Bergner, P. Pareige, B. Radiguet, A. Almazouzi, J. Nucl. Mater. 406 (1) (2010) 84–89, http://dx.doi.org/10.1016/j.jnucmat.2010.05.020.

[6] M.A. Meyers, C. Taylor Aimone, Prog. Mater. Sci. 28 (1) (1983) 1–96. http://dx.doi.org/10.1016/0079-6425(83)90003-8.

[7] V. Lubarda, M. Schneider, D. Kalantar, B. Remington, M. Meyers, Acta Mater. 52 (6) (2004) 1397–1408, http://dx.doi.org/10.1016/j.actamat.2003.11.022.

[8] E. Seppala, J. Belak, R. Rudd, Phys. Rev. B 69(13). http://dx.doi.org/10.1103/PhysRevB.69.134101.

[9] J. Marian, J. Knap, M. Ortiz, Acta Mater. 53 (10) (2005) 2893–2900. http://dx.doi.org/10.1016/j.actamat.2005.02.046.

[10] S. Traiviratana, E.M. Bringa, D.J. Benson, M.A. Meyers, Acta Mater. 56 (15) (2008) 3874–3886, http://dx.doi.org/10.1016/j.actamat.2008.03.047.

[11] R.W. Armstrong, S.M. Walley, Int. Mater. Rev. 53 (3) (2008) 105–128. http://dx.doi.org/10.1179/174328008X277795.

[12] E.M. Bringa, S. Traiviratana, M.A. Meyers, Acta Mater. 58 (13) (2010) 4458–4477. http://dx.doi.org/10.1016/j.actamat.2010.04.043.

[13] L.P. Davila, P. Erhart, E.M. Bringa, M.A. Meyers, V.A. Lubarda, M.S. Schneider, R. Becker, M. Kumar, Appl. Phys. Lett. 86 (16) (2005) 161902, http://dx.doi.org/10.1063/1.1906307.

[14] A.S. Pohjonen, F. Djurabekova, K. Nordlund, A. Kuronen, S.P. Fitzgerald, J. Appl. Phys. 110 (2) (2011) 023509, http://dx.doi.org/10.1063/1.3606582.

[15] H.W. Sheng, M.J. Kramer, A. Cadien, T. Fujita, M.W. Chen, Phys. Rev. B 83(13). http://dx.doi.org/10.1103/PhysRevB.83.134118.

[16] L. Burakovsky, S.P. Chen, D.L. Preston, A.B. Belonoshko, A. Rosengren, A.S. Mikhaylushkin, S.I. Simak, J.A. Moriarty, Phys. Rev. Lett. 104 (25). http://dx.doi.org/10.1103/PhysRevLett.104.255702.

[17] R. Ravelo, T.C. Germann, O. Guerrero, Q. An, B.L. Holian, Phys. Rev. B 88(13). http://dx.doi.org/10.1103/PhysRevB.88.134101

[18] R.E. Rudd, J.F. Belak, Comput. Mater. Sci. 24 (1-2) (2002) 148–153. http://dx.doi.org/10.1016/S0927-0256(02)00181-7.

[19] R.E. Rudd, Phylos. Mag. 89 (34–36) (2009) 3133–3161, http://dx.doi.org/10.1080/14786430903222529.

[20] J. Marian, J. Knap, G. Campbell, Acta Mater. 56 (10) (2008) 2389–2399. http://dx.doi.org/10.1016/j.actamat.2008.01.050.

[21] R. Groger, A. Bailey, V. Vitek, Acta Mater. 56 (19) (2008) 5401–5411. http://dx.doi.org/10.1016/j.actamat.2008.07.018.

[22] S. Xu, Z. Hao, Y. Su, Y. Yu, Q. Wan, W. Hu, Comput. Mater. Sci. 50 (8) (2011) 2411–2421. http://dx.doi.org/10.1016/j.commatsci.2011.03.019.

[23] A.L. Gurson, J. Eng. Mater. Tech. 99 (1) (1977) 2, http://dx.doi.org/10.1115/1.3443401.

[24] G. Collins, H. Melosh, K. Wunnemann, Int. J. Impact. Eng. 38 (6) (2011) 434–439. http://dx.doi.org/10.1016/j.ijimpeng.2010.10.013.

[25] D. Ahn, P. Sofronis, R. Minich, J. Mech. Phys. Solids 54 (4) (2006) 735–755, http://dx.doi.org/10.1016/j.jmps.2005.10.011.

[26] V.A. Lubarda, Int. J. Plast. 27 (2) (2011) 181–200, http://dx.doi.org/10.1016/j.ijplas.2010.04.005.

[27] S. Zhang, J. Zhou, L. Wang, Y. Wang, S. Dong, Mater. Sci. Eng.: A 582 (2013) 29–35, http://dx.doi.org/10.1016/j.msea.2013.06.017.

[28] L.D. Nguyen, D.H. Warner, Phys. Rev. Lett. 108(3). http://dx.doi.org/10.1103/PhysRevLett.108.035501

[29] J. Segurado, J. Llorca, Acta Mater. 57 (5) (2009) 1427–1436, http://dx.doi.org/10.1016/j.actamat.2008.11.031.

[30] M.A. Bhatia, K.N. Solanki, A. Moitra, M.A. Tschopp, Metall. Mater. Trans. A 44 (2) (2012) 617–626, http://dx.doi.org/10.1007/s11661-012-1082-z.

[31] K. Kadau, Science 296 (5573) (2002) 1681–1684, http://dx.doi.org/10.1126/science.1070375.

[32] X.D. Dai, Y. Kong, J.H. Li, B.X. Liu, J. Phys. Cond. Mater. 18 (19) (2006) 4527–4542. http://dx.doi.org/10.1088/0953-8984/18/19/008.

[33] S. Plimpton, J. Comp. Phys. 117 (1) (1995) 1–19, http://dx.doi.org/10.1006/jcph.1995.1039.

[34] P. Erhart, E.M. Bringa, M. Kumar, K. Albe, Phys. Rev. B 72(5). http://dx.doi.org/10.1103/PhysRevB.72.052104.

[35] A. Kubota, M.-J. Caturla, S. Payne, T. Diaz de la Rubia, J. Latkowski, J. Nucl. Mater. 307-311 (2002) 891–894, http://dx.doi.org/10.1016/S0022-3115(02)01008-5.

[36] A. Kubota, D.B. Reisman, W.G. Wolfer, Appl. Phys. Lett. 88 (24) (2006) 241924. http://dx.doi.org/10.1063/1.2210799.

[37] R.E. Rudd, A.J. Comley, J. Hawreliak, B. Maddox, H.-S. Park, B.A. Remington, AIP Cong. Proc. (2012) 1379–1382, http://dx.doi.org/10.1063/1.3686538.

[38] Y. Tang, E.M. Bringa, B.A. Remington, M.A. Meyers, Acta Mater. 59 (4) (2011) 1354–1372. http://dx.doi.org/10.1016/j.actamat.2010.11.001.

[39] Y. Tang, E.M. Bringa, M.A. Meyers, Acta Mater. 60 (12) (2012) 4856–4865, http://dx.doi.org/10.1016/j.actamat.2012.05.030.

[40] C. Ruestes, E. Bringa, A. Stukowski, J. Rodriguez Nieva, G. Bertolino, Y. Tang, M. Meyers, Scripta Mater. 68 (10) (2013) 817–820, http://dx.doi.org/10.1016/j.scriptamat.2013.01.035.

[41] A. Stukowski, Model. Sim. Mater. Sci. Eng. 18 (1) (2010) 015012, http://dx.doi.org/10.1088/0965-0393/18/1/015012.

[42] W. Humphrey, A. Dalke, K. Schulten, J. Mol. Graph. 14 (1) (1996) 33–38, http://dx.doi.org/10.1016/0263-7855(96)00018-5.

[43] A. Stukowski, A. Arsenlis, Model. Sim. Mater. Sci. Eng. 20 (3) (2012) 035012. http://dx.doi.org/10.1088/0965-0393/20/3/035012.

[44] M.A. Meyers, K.K. Chawla, Mechanical Behavior of Materials, Cambridge University Press, Cambridge; New York, 2009.

[45] W.L. Stewart, J.M. Roberts, N.G. Alexandropolous, K. Salama, J. Appl. Phys. 48 (1) (1977) 75, http://dx.doi.org/10.1063/1.323327.

[46] E. Orowan, Proc. Phys. Soc. 52 (1) (1940) 8–22, http://dx.doi.org/10.1088/0959-5309/52/1/303.

[47] J.W. Swegle, D.E. Grady, J. Appl. Phys. 58 (2) (1985) 692, http://dx.doi.org/10.1063/1.336184.

[48] H. Quinney, G.I. Taylor, Proc. R. Soc. Lond. 163 (913) (1937) 157–181, http://dx.doi.org/10.1098/rspa.1937.0217.

[49] V. Vitek, Prog. Mater. Sci. 56 (6) (2011) 577–585, http://dx.doi.org/10.1016/j.pmatsci.2011.01.002.

[50] E.M. Bringa, K. Rosolankova, R.E. Rudd, B.A. Remington, J.S. Wark, M. Duchaineau, D.H. Kalantar, J. Hawreliak, J. Belak, Nat. Mat. 5 (10) (2006) 805–809, http://dx.doi.org/10.1038/nmat1735.

[51] N.R. Barton, J.V. Bernier, R. Becker, A. Arsenlis, R. Cavallo, J. Marian, M. Rhee, H.-S. Park, B.A. Remington, R.T. Olson, J. Appl. Phys. 109 (7) (2011) 073501, http://dx.doi.org/10.1063/1.3553718.

[52] S. Nemat-Nasser, J.B. Isaacs, M. Liu, Acta Mater. 46 (4) (1998) 1307–1325. http://dx.doi.org/10.1016/S1359-6454(97)00746-5.

[53] L.L. Hsiung, J. Phys. Cond. Mater. 22 (38) (2010) 385702, http://dx.doi.org/10.1088/0953-8984/22/38/385702.

[54] J.N. Florando, N.R. Barton, B.S. El-Dasher, J.M. McNaney, M. Kumar, J. Appl. Phys. 113 (8) (2013) 083522, http://dx.doi.org/10.1063/1.4792227.

[55] J. Hagelaar, E. Bitzek, C. Flipse, P. Gumbsch, Phys.Rev.B 73 (4). http://dx.doi.org/10.1103/PhysRevB.73.045425.

[56] V.A. Lubarda, Int. J. Solid Struct 48 (5) (2011) 648–660, http://dx.doi.org/10.1016/j.ijsolstr.2010.11.006.